The Analysis and Digital Signal Processing of NOAA's Surface Current Mapping System

JAMES A. LEISE

Abstract—We describe newly developed numerical procedures used to analyze and process sea-echo data acquired with National Oceanic and Atmospheric Administration's (NOAA) dual-site HF-radar system called Coastal Ocean Dynamics Applications Radar (CODAR). CODAR is a transportable shore-based system that can map surface currents out to a nominal range of 50 km. Since its introduction in 1976, it has performed well in a dozen major experiments. Until recently, however, the data processing was labor intensive, difficult to understand, and slow. The processing presented here largely corrects these difficulties, giving CODAR reliable real-time mapping capabilities.

I. INTRODUCTION

THE SEA SURFACE is nearly ideal for remote sensing; it is accessible to radio waves from above; it is dynamically linked to fluid motions below. For this reason, radars are particularly valuable as observational tools; they can, in principle, provide complete and instantaneous pictures of the ocean surface. CODAR is one such tool, a measurement tool designed to map surface currents in coastal zones [1].

The scattering mechanism underlying CODAR and, more generally, all HF radar oceanography was discovered by Crombie [2] more than 25 years ago. He observed that most sea echo (backscatter) is a form of Bragg scatter resulting from resonant wave trains lining up to form a diffraction grating. These observations were later confirmed theoretically by Wait [3] and Barrick [4]. Since then HF radars have been developed to measure surface currents, wind directions, and wave heights from Doppler-shifted Bragg scatter. These basic HF measurements have been discussed in a review article by Barrick [5], and more recently, for sky-wave radars by Georges [6].

A novel feature of the CODAR system is its use of a 4-element phased-array receive antenna to determine the direction of incident backscatter. This antenna is a more advanced version of a 2-element antenna employed by Crombie [7] to measure sea-echo from the Gulf Stream. The advantage of such antennas is that they are compact in size for the angular resolution they offer; because of this, CODAR is transportable.

Perhaps the most distinctive aspect of CODAR is the manner in which sea echo is ultimately converted into vector maps. Operationally, there are radial and vector mapping steps. The radial processing converts Doppler sea echo into polar maps; this can be done independently at each of the two radar sites.

The vector processing, on the other hand, requires radial data from both sites.

Work on this processing was initiated by Barrick and Weber [1], [8] in about 1976. Since that time, the processing models and numerical procedures have evolved and changed considerably. This paper is, basically, an account of improved methods used to process CODAR data. The material is roughly organized as follows.

- We describe how valid first-order Doppler shifts are automatically identified and how the corresponding directions of incident backscatter are determined.
- We show how radial maps are numerically synthesized from measured Doppler shifts and computed directions of incident backscatter.
- We show how a vector current map is finally computed from two radial velocity maps.
- We check our processing by comparing CODAR data with current-meter data taken off the coast of northern California as part of the Coastal Ocean Dynamics Experiment (CODE-1 experiment).[1]

Errors occurring at the different processing levels are studied. In particular, an error measure for determining angular resolution is presented. For CODE-1 data, the deduced angular errors are found to lie in the range of 5–10°. Also, during CODE-1 the mean radial-velocity difference between CODAR data and current-meter data is found to be less than 5 cm/s over a 2-week period. We conclude that our processing works well.

II. SIGNAL DETECTION

Each of CODAR's two sites is an HF radar (nominally, 25.4 MHz) consisting of a broad-beam transmit antenna, a 4-element receive antenna together with a minicomputer controlled data acquisition and processing system.

Briefly, each site records ground-wave sea echo resulting when transmitted pulses interact with waves on the ocean surface. The backscatter is then gated in time, demodulated, and quantized to produce complex time-series records. One such record is saved for each of the four antenna elements and for each of the time-gated circular range cells shown in Fig. 1. (At present, 4 × 57 multiplexed records consisting of 1024 points each can be acquired in about 4 1/2 min of operation.) A more detailed account of the hardware and data acquisition is available in [1].

---

[1] Coastal Ocean Dynamics Experiment, a 2-year multiorganizational program funded in part by NASA to understand the role of the wind in forcing circulation over the continental shelf.
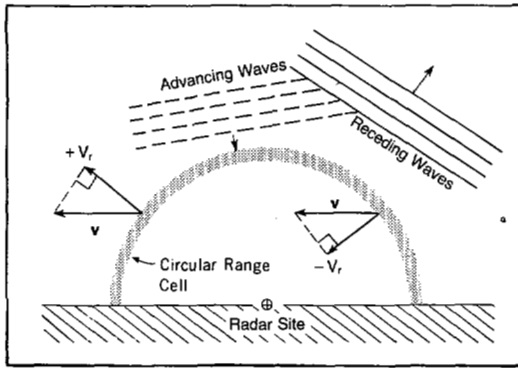
Fig. 1. CODAR backscatter geometry. Transmitted broad-beam pulses interact with Bragg-resonant wave trains traveling radially in many directions. The returned sea echo from a circular range cell consists of convolved Doppler-shifted radial velocity data ($\pm V_r$).

Fig. 2. A typical CODAR spectrum. Only first-order sea echo can be used to compute current velocities from the Doppler shifts.

Subsequently, the time-series records are statistically edited to remove spurious spikes due to interference or hardware failure, detrended in the time domain to remove near-dc components, and spectrally analyzed with a fast Fourier transform. Details of these procedures can be found in [9]. For present purposes the resulting complex spectral records constitute the basic output of CODAR.

A typical sea-echo spectrum is illustrated in Fig. 2. There are two prominent sidebands, an advancing sideband on the right and a receding sideband on the left. One of Crombie's [2] early findings was that these sidebands were due to Bragg scatter from resonant wave trains propagating directly toward or away from the radar; he established the resonance condition $L = \lambda/2$ where L is the distance between wave crests and λ is the radar wavelength. The resonant backscatter, in turn, determines the Bragg lines $f^{\pm} = \pm\sqrt{g/\pi\lambda}$ shown in Fig. 2 where g is the acceleration of gravity. In a later paper [7], Crombie further showed that Bragg scatter gets Doppler shifted away from the Bragg lines when the wave trains are transported by currents. It is this shift that HF radars measure; it is from this shift that radial current velocities are deduced.

The purpose of signal detection is to isolate the resonant peaks produced by Doppler-shifted scatter. These peaks are called first-order sea echo and occupy regions of finite width as shown in Fig. 2. Adjacent to the first-order regions are second-order regions caused by wave–wave interactions [10], [11]. The second-order echo is known to produce erroneous results and, consequently, must be excluded from the processing.

One of the improvements in our signal detection over earlier versions [8] is that the signal-to-noise ratio is estimated using the second-order regions to compute the noise. This helps in separating first-order return from second-order return. Another improvement is that the two sidebands are treated independently; it is possible for the second-order energy in one sideband to exceed the first-order energy in the other.

The specific algorithm used is a two-part procedure developed by Miller and Leise [12]. It is applied to the combined energy spectrum of the four antenna elements (fixed range). First, mean positions are located with a centroid-estimation technique and then the first-order return is separated from the second-order return with a local-thresholding method.
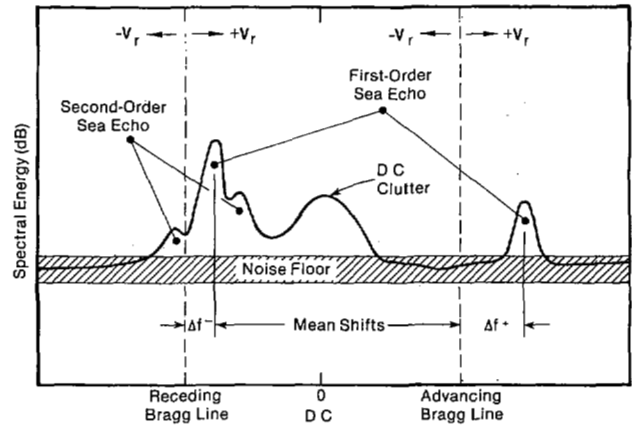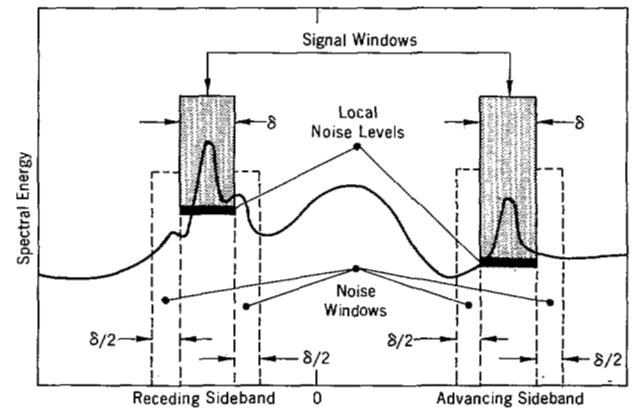

Fig. 3. Basic signal detection. The signal windows are positioned with a centroid-estimation algorithm. Local noise levels are computed from the noise windows and high-energy signals are found with a local-thresholding scheme.

This is illustrated in Fig. 3. Shown are two signal windows of width δ centered around points supplied by the centroid-estimation algorithm. Each local-noise level represents the average energy in the two adjacent noise windows. Data in the signal windows are then thresholded by requiring the spectral energies to be given a number of decibels above their respective noise levels.

The spread δ is an important sea-state parameter needed to automatically process CODAR data. There is a strong dependence on oceanographic environment; features such as maximum velocities and topography seem to be strong influences. However, strong temporal dependence has not been observed; to date, one setting per location has proved adequate. Nominal values have ranged between 100 and 500 cm/s.

Computed signal windows for three combined spectra taken with CODAR during CODE-1 (Site 2 in Fig. 10) are shown in Fig. 4. (In this experiment, each site measured 31 ranges spaced 1.2 km apart.) These spectra are 1024 points long with a Doppler velocity resolution of 2.2 cm/s. Therefore, the spread of 150 cm/s corresponds to 68 spectral Doppler frequencies. Of particular interest is the interference (of unknown origin) appearing in the middle spectrum ($R = 19.8$ km) of Fig. 4. In spite of its similarity in size and shape to the first-order regions, it did not confuse our signal-detection algorithm.
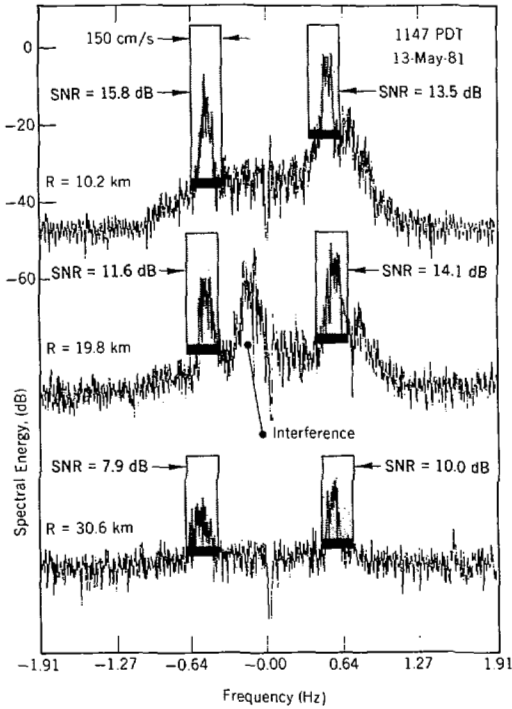
Fig. 4. Representative spectra from a data set taken during CODE-1. The SNR values were computed from the ratio of total energies in the signal windows to total energies in the adjacent noise windows (see Fig. 3). The interference shown did not confuse the signal-detection algorithm.

Fig. 5. Geometry of CODAR's 4-element phased-array antenna. The response pattern is a histogram of recovered angle ϕ showing how the single-angle computation performs in white noise. It shows that angles along the antenna diagonals are preferred.

Finally, local thresholding is used to separate out the strongest signals. If the thresholding level is set too low, noise could be misinterpreted as valid data; if it is set too high, valid data could be discarded. To illustrate sensitivity, the total data set represented by Fig. 4 ($\delta = 150$ cm/s) has a total of 5216 points in the various signal windows. Of these 55 percent lie above a 3-dB level (i.e., 3 dB above the local noise levels), 41 percent lie above a 6-dB level, and only 28 percent lie above a 10-dB level.

III. DIRECTION FINDING

Mathematically, the determination of source characteristics from given backscatter data is classified as an inverse problem [13]. Such problems are usually ill-posed and lack unique solutions because there are more degrees of freedom in the backscatter than can be accurately measured. This is one of the basic problems that CODAR processing must solve; the angular distribution of incident backscatter must be estimated from phased-array antenna data.

Direction-finding methods for computing incidence angles have generally been favored over beam-steering methods because of greater computational efficiency. Crombie [7] first analyzed sea echo with a 2-element antenna; it could uniquely resolve a single angle over 180° of azimuth. Initially [8], CODAR employed a three-element antenna which was later replaced with a 4-element antenna [1], [14]. In principle, both these antennas could resolve two incidence angles over 180° and 360° of azimuth respectively. However, for either antenna, the computation of two angles has the serious defect of becoming singular in the important special case when the in-
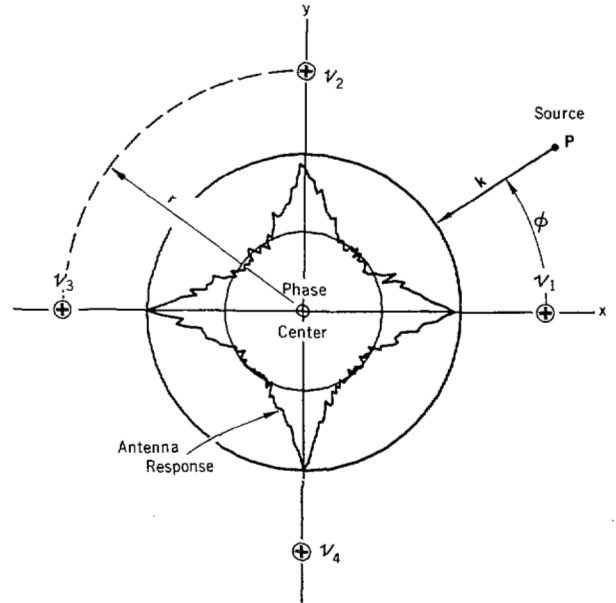
cident backscatter is coming from predominantly one direction. This, in turn, makes dual-angle computations difficult to analyze and implement. For this reason, we here use a single-angle computation which is much more stable; it can uniquely resolve one angle over 360° of azimuth.

The geometry of our 4-element array is shown in Fig. 5. The demodulated voltages excited by a single plane wave of complex amplitude A and incidence angle ϕ are

$$U_k = A e^{iR \cos [\phi - (k-1)\pi/2]}, \quad k = 1, 2, 3, 4 \qquad (1)$$

where $R = 2\pi r/\lambda$ is the electrical radius, r is the physical radius, and λ is the radar wavelength. The single-angle computation then consists of computing an estimate $\hat{\phi}$ as follows:

Step I:

$$\sigma_s = U_1 U_4{}^* + U_3{}^* U_2 \qquad \sigma_c = U_1 U_2{}^* + U_3{}^* U_4 \qquad (2)$$

Step II:

$$s(\hat{\phi}) = \text{ATAN2} \, [\text{Im} \, (\sigma_s), \text{Re} \, (\sigma_s)]$$

$$c(\hat{\phi}) = \text{ATAN2} \, [\text{Im} \, (\sigma_c), \text{Re} \, (\sigma_c)] \qquad (3)$$

Step III:

$$\hat{\phi} = \text{ATAN2} \, (s(\hat{\phi}), \ c(\hat{\phi})) - \pi/4 \qquad (4)$$

where asterisks denote complex conjugation and ATAN2 is the (Fortran) inverse tangent (valid over 360°). Also Re (σ) and Im (σ) denote the real and imaginary parts of σ. Note that this computation can be applied to any set of voltages whether or not they satisfy our model (1). However, when they do satisfy the plane-wave model (1), we get the correct incidence angle $\hat{\phi} = \phi$.

This algorithm possesses a number of important features. First, it is stable to voltage amplitude imbalances; in fact, for a single plane wave, the computation is valid even when one of the voltages is set to zero! Second, the electrical radius R cancels the inverse tangent of (4) and, consequently, ϕ does not explicitly depend on R. However, to avoid aliasing, R must be less than $\pi/\sqrt{2}$. Presently, the CODAR system uses somewhat less than a quarter-wavelength radius ($r < \lambda/4$) and so the electrical radius ($R < \pi/2$) is safely within this range. Third, the computation is statistically nonuniform as shown by the response pattern of Fig. 5 which is a histogram of estimated angle ϕ and shows how the computation responds when the real and imaginary parts of the voltages are generated from white noise. The nonuniformity of this pattern tells us that noise tends to bias the single-angle computation toward the antenna diagonals.

Errors in the single-angle computation can be routinely monitored through the use of trigonometric statistic T defined

$$T = [s^2(\hat{\phi}) + c^2(\hat{\phi})]/2R^2 \tag{5}$$

because when the voltages satisfy the single-angle model, T is always unity. However, a more useful and reliable quantity is the normalized statistic $\tau = \Delta_T/\overline{T}$ computed from an ensemble with sample mean $\overline{T}$ and standard deviation Δ_T. What makes this normalization desirable is that it is independent of the electrical radius R (like the estimate ϕ). Thus for a fixed antenna radius, the radar wavelength λ can, in particular, be varied without altering this quotient.

These statistics can be correlated with angle errors as shown in Fig. 6 through the use of a noise model. The model used simply assumes that the SNR values of the antenna elements are the same. Thus received voltages are simulated as unit-amplitude plane waves to which noise of relative amplitude ϵ is added:

$$U_k = e^{iR\cos[\phi - (k-1)\pi/2]} + \epsilon e^{i\theta_k}, \quad k = 1, 2, 3, 4 \tag{6}$$

where $R = \pi/2 (r = \lambda/4)$.

The data for the two curves of Fig. 6 were generated with Monte Carlo integrations. A trial for a fixed noise level ϵ consisted of the following sequence of steps:

- randomly choose ϕ, θ_k, and simulate voltages U_k from (6),
- compute an estimate $\hat{\phi}$ from (4) together with the error $E = \hat{\phi} - \phi$,
- compute the statistic T from (5).

In turn, for each fixed ϵ, the statistics Δ_T and τ together with the rms-angle error were computed from an ensemble of many trials. By considering ϵ as a dummy parameter, we are left with a dependence between the trigonometric statistics and the rms-angle errors; this is the dependence shown in Fig. 6. Because the voltage model (6) has five degrees of freedom (with ϵ fixed), approximately 500 000 trials were required for each ϵ to get the statistics to converge to graphical accuracy (~3 digits). Also, 70 values of ϵ ranging from 0.01 to 0.7 were used.
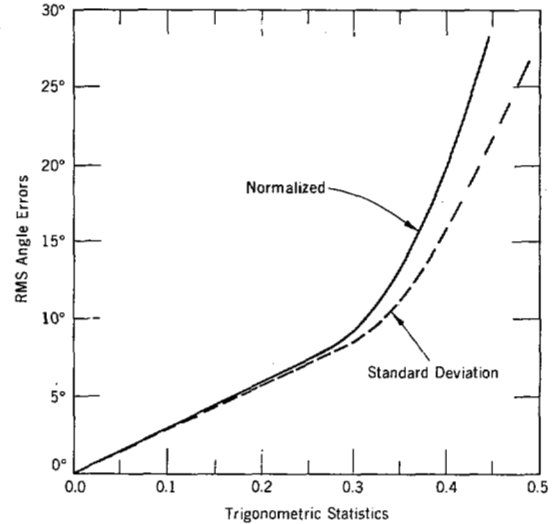

Fig. 6. Error curves for direction finding. These curves relate measurable trigonometric statistics Δ_T and τ with angle errors.

Finally, when applied to CODAR data, these statistics are computed from the ensemble of points remaining after signal detection. For example, when the data set represented by Fig. 4 (see Section II) is thresholded at 3-, 6-, and 10-dB levels, the normalized statistics τ are 0.36, 0.33, and 0.31 for the receding sideband, and 0.28, 0.24, and 0.21 for the advancing sideband. Thus the trigonometric statistics decrease with an increasing SNR value as expected from theory. In turn, when these statistics are checked against the error curve of Fig. 6, we are led to the conclusion that data processed in this way has nominal angle errors ranging between 5° and 10°—a result useful for constructing radial maps.

IV. RADIAL MAP SYNTHESIS

We begin by reviewing material pertinent to constructing a radial map.

- The data for each (time-gated) range R consists of the four antenna spectra $U_k(f)$, $k = 1, 2, 3, 4$.
- Frequencies f of high-energy first-order sea echo are obtained by applying signal detection to the averaged energy spectrum

$$e(f) = \frac{1}{4} \sum_{k=1}^{4} |U_k(f)|^2. \tag{7}$$

- For each frequency f of first-order return, an angle $\hat{\phi}(f)$ is estimated by applying the single-angle computation (4) to the voltages $U_k(f)$, $k = 1, 2, 3, 4$.
- For each frequency f of first-order return, a radial velocity $V(f) = \lambda \Delta f/2$ is computed from its Doppler shift Δf relative to the respective Bragg line (see Fig. 2).

In short, for each frequency f of first-order return there is a polar-grid point $(R, \hat{\phi}(f))$ and a radial current velocity $V(f)$; the polar-grid point locates the source of incident backscatter, and the velocity $V(f)$ is attached to that point. A radial veloc-

ity "map" then results from the totality of velocities obtained by scanning the first-order frequencies through all ranges. Such maps are statistically nonuniform insofar as the computed directions of incident backscatter tend to cluster more densely in some angular regions. There are several reasons for this. First, sea echo is naturally stronger in certain directions (generally strongest in the wind direction). Second, the strength of return for a given direction can be statistically random (in time) due to the statistically random nature of the sea surface. Third, the single-angle computation is statistically nonuniform in the presence of noise as was shown in Fig. 5.

This nonuniformity causes complications when angles are quantized. Specifically, azimuth angles are quantized into N equal angle bins of width $\Delta\theta = 2\pi/N$ and centers $\theta_k = (k - 1)\Delta\theta$, $(k = 1, 2, \cdots, N)$. A computed angle $\hat{\phi}$ then falls in the kth angle bin if it satisfies

$$\theta_k - \Delta\theta/2 \leqslant \hat{\phi} < \theta_k + \Delta\theta/2 \qquad (8)$$

and the corresponding Doppler velocity is assigned the bin index k. If several radial velocities result in the same angle-bin index, the respective Doppler velocities are weighted with their corresponding energies (7) thereby giving preference to the stronger signal.

The difficulty is in choosing $\Delta\theta$; good azimuthal resolution requires a large number N of angle bins. However, because there are a limited number of first-order points, increasing N results in less uniform coverage. In the extreme case where there are more bins than points, some bins must be left empty and a nonuniform distribution results. We conclude that optimal processing requires the angle-bin width $\Delta\theta$ to roughly match the angular resolution of the radar. It is here that the rms-angle errors of Fig. 6 are particularly valuable.

In the preceding section, we learned (from the trigonometric statistic τ) that the data set represented by the spectra of Fig. 4 produced nominal angle errors of between 5° and 10°. A radial map for 10° angle bins is shown in Fig. 7. This map is essentially a Mercator projection of angle versus range; the rows represent ranges spaced 1.2 km apart with the first positioned at 1.8 km; the columns represent discrete angle bins spaced 10° apart. Furthermore, each number on the map represents a radial velocity given in units (10.2 cm/s) above or below the mean (4.5 cm/s); asterisks denote overflow. Thus the dynamic range (−5 to 5) of numbers shown represents radial velocities between about −46 and +55 cm/s.

Next, because the shoreline was nearly straight (see Site 2 in Fig. 10), the sector denoted land at the top of the map is 180° wide and comprises 50 percent of the total possible points (1116). However, only 41 percent (456) of the total bins are filled and of these 5 percent (25) fall on land. These statistics deteriorate notably when $\Delta\theta$ is decreased; the 41 percent coverage for 10° bins becomes a 33-percent coverage for 5° bins and a 20 percent-coverage for 2° bins. We conclude that 10° bins are about right.

V. VECTOR MAP SYNTHESIS

The last level of processing is basically geometric; radial velocities from two sites are combined to form a vector map.
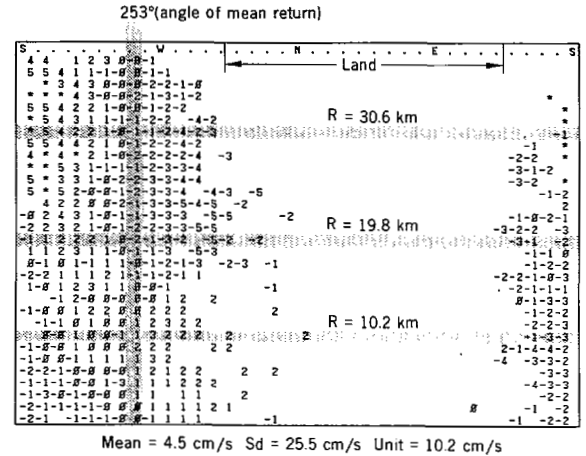

Fig. 7. A CODE-1 radial map computed with a spread of 150 cm/s, a thresholding level of 6 dB, and angle bins of 10°. The rows are ranges spaced 1.2 km apart. The numbers represent radial velocities in units above or below the mean; asterisks indicate overflow. The shaded rows were computed from the CODE-1 spectra shown in Fig. 4.

However, before radial data can be combined, the data must be interpolated to a common grid. To do this, we represent a rectangular grid point (x, y) in polar form (r, θ) relative to each of the respective sites. For a given site, the radial distance r to (x, y) must lie between two discrete ranges and θ must lie between two discrete bin angles, that is, for some i and j

$$R_i \leqslant r < R_{i+1} \qquad \theta_j \leqslant \theta < \theta_{j+1}. \qquad (9)$$

The point (r, θ) is, therefore, surrounded by radial velocity data $(V_{k,l}: k = i, i + 1; l = j, j + 1)$—the four nearest neighbors. These velocities serve as the data base for interpolation.

Following Miller and Strauch [15], we use linear bivariate interpolation (also bilinear Lagrange interpolation) to estimate a radial velocity $V(x, y)$ at the Cartesian grid point (x, y). With the normalized variables

$$\hat{r} = \frac{r - R_i}{R_{i+1} - R_i} \qquad \hat{\theta} = \frac{\theta - \theta_j}{\theta_{j+1} - \theta_j} \qquad (10)$$

this interpolation is compactly expressed

$$V(x, y) = (1 - \hat{r})(1 - \hat{\theta})V_{i,j} + (1 - \hat{r})\hat{\theta}V_{i,j+1}$$
$$+ \hat{r}(1 - \hat{\theta})V_{i+1,j} + \hat{r}\hat{\theta}V_{i+1,j+1}. \qquad (11)$$

If any of the four pieces of radial velocity data $V_{k,l}$ is missing, the interpolation is simply omitted and $V(x, y)$ is undefined.

This interpolation has several desirable properties. First, it is stable insofar as no interpolate can exceed (in magnitude) the data base values; this is a result of linearity. Second, the totality of interpolation functions (11) (one for each cell) pieces together to form a continuous spline [16], that is, a continuous, piecewise-linear surface (like a geodesic dome) passing through the given data base of radial velocities.

It is from such interpolation surfaces that the radial velocities $V_1(x, y)$ and $V_2(x, y)$ are obtained for the respective
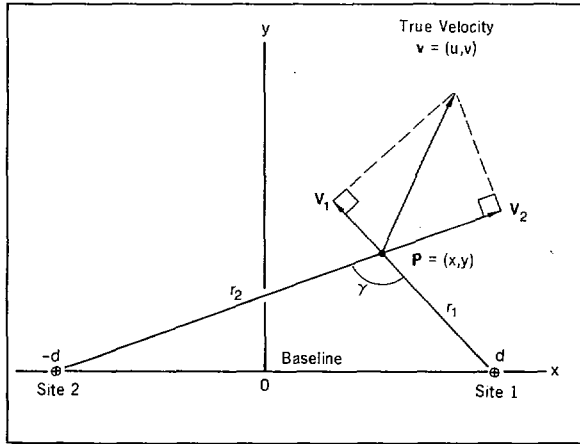
Fig. 8. Two-site radar geometry. As the triangulation angle γ is increased, the computation of the total vector velocity $\bar{v}$ from the radial data V_1 and V_2 becomes unstable.

Fig. 9. Error curves obtained by incrementing cos (γ) (see Fig. 8) in steps of ±0.2. These curves show how a velocity error ϵ gets amplified as the triangulation angle deteriorates.

sites. With the geometry of Fig. 8 these velocities are inverted to give the Cartesian vector $\bar{v} = (u, v)$ where

$$u = \frac{r_2 V_2 - r_1 V_1}{2d} \qquad v = \frac{r_1 V_1(x+d) - r_2 V_2(x-d)}{2yd} .$$

(12)

Here, $2d$ is the distance between sites and r_k is the distance of the kth site to the inversion point (x, y). It should be noted that as y becomes small or x becomes large, the calculation of v becomes unstable.

These instabilities are inherent shortcomings of radial measurement. Along the baseline, both sites measure the same radial component; the transverse component cannot be sensed. Consequently, only one degree of freedom is measured and the vector inversion breaks down. Similar instability in u exists at large distances from the sites. Inversion errors have been analyzed in detail by Leise [17]. Results show a dependence on the triangulation angle γ (see Fig. 8) of the two intersecting radial lines. Specifically, velocity errors ϵ are amplified by the inversion as follows:

$$\text{Error } (\gamma) = \begin{cases} \epsilon/\sqrt{2} \, |\sin (\gamma/2)|, & \gamma \leqslant \pi/2 \\ \epsilon/\sqrt{2} \, |\cos (\gamma/2)|, & \gamma \geqslant \pi/2. \end{cases}$$

(13)

Error levels are shown in Fig. 9; each curve is a contour of constant triangulation angle. These curves are useful for assessing the integrity of CODAR vector maps.

Fig. 10 is a map of vectors falling within the 2ϵ region of Fig. 9; points outside this region were automatically deleted as unstable. The unshaded portion is the basic vector map; it was constructed directly from the (sparse) CODE-1 radial map of Fig. 7 (Site 2) together with a similar radial map for the companion site (Site 1).

The shaded portion of the vector map is a numerical extension and corresponds to those points for which there were missing radial data in one of the two interpolations (11) needed for the vector inversion (12). (If any one of the eight pieces of needed radial velocity data is missing, the vector is undefined.)
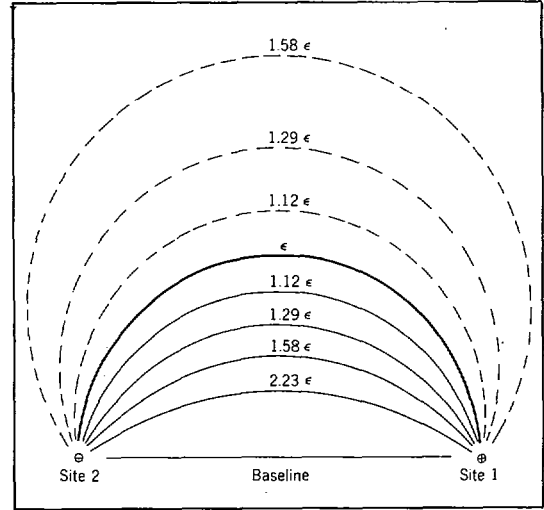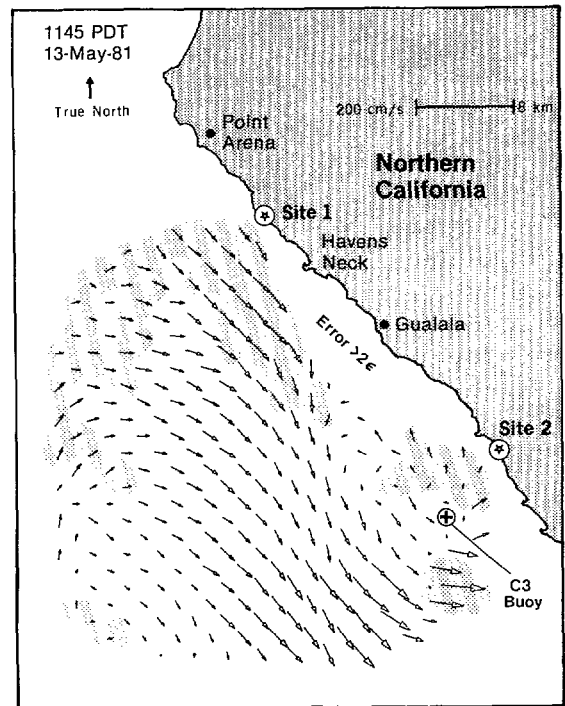

Fig. 10. A CODE-1 vector map. The distance between Site 1(38°50′ N, 123°38′W) and Site 2 (38°40′N, 123°25′W) is about 28 km. The heart shape of the map is primarily due to range limits (~40 km). The radial processing was the same for both sites (see Fig. 7). The shaded regions of this map are numerical extensions.

One way to deal with missing data is to change interpolation methods. However, because of the unpredictable nature of the radial maps, this strategy leads to many formulas for many situations. Different methods respond unequally to different scales and have different stability properties; in turn, the resulting interpolation surfaces could be badly discontinuous. Conceptually, the direct way to deal with missing data is simply to complete or extend the needed parts of the radial maps. This is done with a numerical averaging scheme [18]; it is implemented by iteratively replacing missing data for different scale
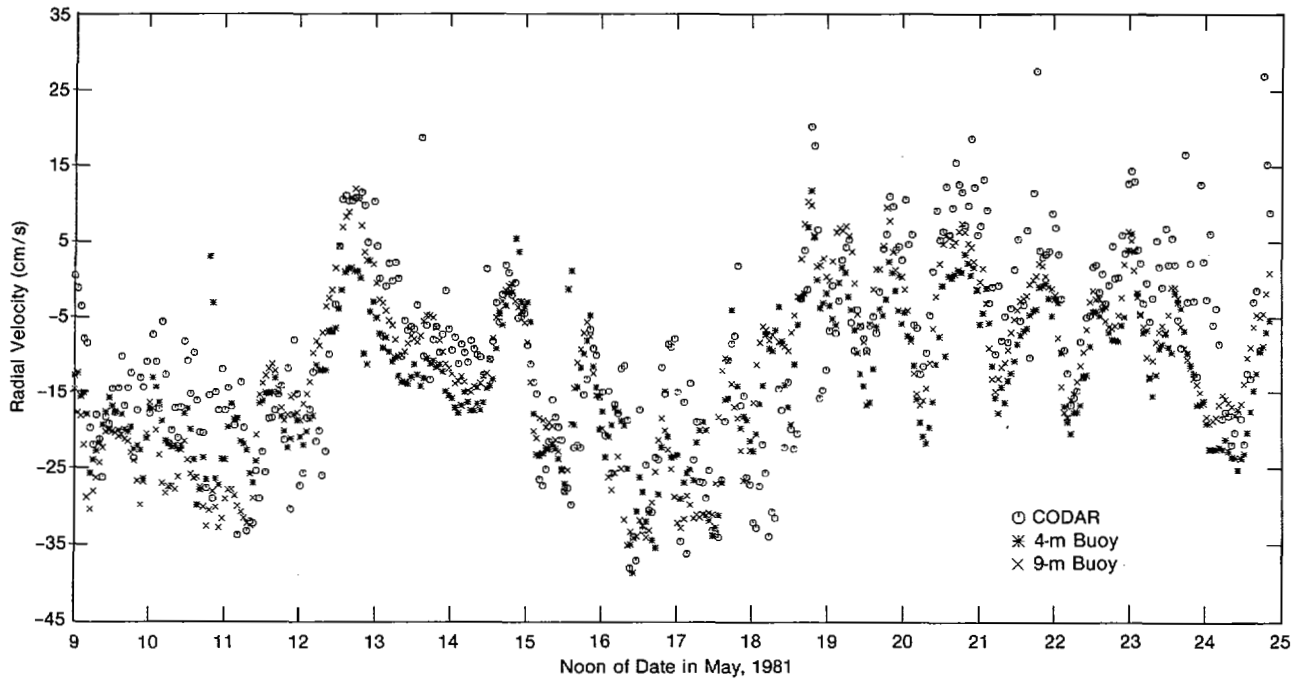
Fig. 11.   A 2-week radial velocity comparison of CODAR Site 2 data with current-meter data taken at 4- and 9-m depths.
The current meters were part of the C3 data buoy shown in Fig. 10.

sizes. It has produced good consistent results; when the 10° map of Fig. 10 was processed with 2° and 5° angle bins, all vector maps were similar. Also, these vector maps were in good agreement with those obtained by first averaging several radial maps together (to help reduce the number of missing values).

VI. EXPERIMENTAL RESULTS

Our processing has been successfully tested on a variety of data sets. As one example, it has been applied to study CODE-1 data taken over a 2-week period of May 1981; enough data were acquired by CODAR to produce a map every 15 min. The two sites shown in Fig. 10 were spaced about 28 km apart and the range of the radars was about 40 km; the heart shape of the vector map is due to this range limit together with the triangulation error constraint described in the preceding section.

The thirteenth of May was of special interest because the wind stopped blowing on that day revealing an eddy or back-flow in front of Site 2 (see Fig. 10). Prior to this, a wind of about 10 m/s blew parallel to the continental shelf (from the NW) forcing a near uniform surface current in the same direction.

An important comparison was provided by data from a buoy located about 7.5 km offshore in front of Site 2 (C3 in Fig. 10). Specifically, the radial surface currents (offshore drift) as measured by Site 2 are compared against data from current meters at 4- and 9-m depths. Hourly samples for the 2-week period are shown in Fig. 11. (CODAR data were processed by averaging four radial maps over each hour.) It is interesting to note that prior to the 13th the three measurements are poorly correlated, suggesting wind-induced mixing. However, when the wind subsided on the 13th, the three measurements correlated well, suggesting laminar flow.

Also, over this 2-week period, the mean and standard deviation of the difference between measurements of offshore drift were:

- (4-m current meter) − (CODAR data)
  Mean = −4.25 cm/s, SD = 9.39 cm/s.
- (9-m current meter) − (4-m current meter)
  Mean = 1.25 cm/s, SD = 6.64 cm/s.

Therefore, in the mean, CODAR agrees with the 4-m current meter to within 5 cm/s. The somewhat greater standard deviation between CODAR and the 4-m current meter is, no doubt, evidence that the surface region is more subject to fluctuations than the interior. Everything considered, this is a very favorable check on our processing.

ACKNOWLEDGMENT

REFERENCES

[1] D. E. Barrick, M. W. Evans, and B. L. Weber, "Ocean surface currents mapped by radar," *Science*, vol. 198, pp. 138–144, 1977.
[2] D. D. Crombie, "Doppler spectrum of sea echo at 13.56 Mc/s," *Nature*, vol. 175, pp. 681–682, 1955.
[3] J. R. Wait, "Theory of HF ground wave backscatter from sea waves," *J. Geophys. Res.*, vol. 71, pp. 4839–4842, 1966.
[4] D. E. Barrick, "First-order theory and analysis of MF/HF/VHF scatter from the sea," *IEEE Trans. Antennas Propagat.*, vol. AP-20, pp. 2–10, Jan. 1972.
[5] ——, "HF radio oceanography—A review," *Bound.-Layer Meteorol.*, vol. 13, pp. 23–43, 1978.
[6] T. M. Georges, "Progress toward a practical Skywave sea-state radar," *IEEE Trans. Antennas Propagat.*, vol. AP-28, pp. 751–761, Nov. 1980.
[7] D. D. Crombie, "Resonant backscatter from the sea and its application to physical oceanography," in *Proc. of the IEEE Ocean '72 Conf.*, IEEE Publ. 72CHO 660-1 OCC, 1972, pp. 173–179.

[8] D. E. Barrick and M. W. Evans, "Implementation of coastal current-mapping HF radar system, Progress Report No. 1," National Oceanic and Atmospheric Administration (NOAA), Boulder, CO, Tech. Rep. ERL 373-WPL 47, 1976.

[9] J. A. Leise, "A segmented editing and detrending method for discrete Fourier transforms," NOAA, Boulder, CO, Tech. Memo. ERL WPL-83, 1981.

[10] B. L. Weber and D. E. Barrick, "On the nonlinear theory for gravity waves on the ocean's surface, Part I: Derivations," *J. Phys. Oceanog.*, vol. 7, pp. 3–10, 1977.

[11] D. E. Barrick, "The ocean waveheight nondirectional spectrum from inversion of the HF sea-echo Doppler spectrum," *Remote Sens. Environ.*, vol. 6, pp. 201–227, 1977.

[12] P. A. Miller and J. A. Leise, "Radar Doppler detection methods with applications to CODAR," NOAA, Boulder, CO, Tech. Memo. ERL WPL-94, 1982.

[13] R. G. Newton, "Inverse problems in physics," *SIAM Review*, vol. 12, no. 3, pp. 346–356, 1970.

[14] B. L. Weber and J. A. Leise, "A four-element direction-finding antenna," NOAA, Boulder, CO, Tech. Memo. ERL WPL-99, 1982.

[15] L. J. Miller and R. G. Strauch, "A dual Doppler radar method for the determination of wind velocities within precipitating weather systems," *Remote Sens. Environ.*, vol. 3, pp. 219–235, 1974.

[16] P. M. Prenter, *Splines and Variational Method*. New York: Wiley, 1975, 323 pp.

[17] J. A. Leise, "Radar geometry of surface velocity maps," NOAA, Boulder, CO, Tech. Memo. ERL WPL-93, 1982.

[18] ——, "A multidimensional scale-telescoped filter and data extension package," NOAA, Boulder, CO, Tech. Memo. ERL WPL-82, 1981.

★

James A. Leise was born in Hollywood, CA, on February 11, 1943. He received the B.S, M.S., and Ph.D. degrees in mathematics from the University of Colorado, Boulder, in 1966, 1968, and 1972, respectively.

From 1972 to 1975 he taught Mathematics at the University of Wisconsin, Milwaukee, and at the University of Colorado. Between 1975 and 1977 he worked for the Cooperative Institute for Research in the Environmental Sciences (CIRES), Boulder, CO. Since 1977, he has been with the Wave Propagation Laboratory, National Oceanic and Atmospheric Administration in Boulder, CO. His publications include work in oceanography, meteorology, lightning theory, digital signal processing, antenna theory, scattering theory, and algebraic topology. His primary interest is in combining physical equations with numerical methods to process and analyze scientific data.